The Innovation, Volume *2*

Supplemental Information

Direct conversion of CO_2 to a jet fuel over CoFe alloy catalysts

Lei Zhang, Yaru Dang, Xiaohong Zhou, Peng Gao, Alexander Petrus van Bavel, Hao Wang, Shenggang Li, Lei Shi, Yong Yang, Evgeny I. Vovk, Yihao Gao, and Yuhan Sun

Supplemental Materials and Methods

Catalyst preparation. CoFe-*x*Na catalysts prepared from CoFe-LDH materials were synthesized with atomic ratios of Co^{2+}:Fe^{3+} = 2. All the LDH precursors were fabricated by co-precipitation at room temperature. The mixed solution of Co/Fe nitrate salts (0.5 mol L^{-1}) and the mixed solution of Na_2CO_3 and NaOH (1 mol L^{-1}) were added simultaneously, and the pH value was controlled in 10. After the precipitate was aged for 15 hours at 70°C, the filter cake was obtained by centrifugation and washing. Derived product was placed in the oven at 100 ºC for 14 h to obtain various CoFe-LDH samples. The CoFe-*x*Na catalysts were prepared by calcination of the corresponding precursors in muffle furnace at 500 ºC for 4 h. The sodium concentration of CoFe-*x*Na catalysts was controlled by adjusting the total amounts of water during filtration and washing steps. CoFe-LDH precursors of CoFe-0.81Na were suspended in DMF and placed in an ultrasonic bath under stirring. Samples were sonicated for 6 h and then filtered and calcined at 500 ºC to obtain CoFe-0.82Na-U. Co-0.63Na, Co, Fe-0.67Na, Fe and CoFe/Al_2O_3-1.09Na catalysts were synthesized without the iron or cobalt nitrite solution or with the aluminum nitrite solution (Co^{2+}:Fe^{3+}:Al^{3+} = 2:1:0.6) at otherwise the same conditions. Pure CoFe, Co and Fe samples were obtained by washing the precursors 50 times before calcination.

Catalyst characterization. The metal composition of various samples was analyzed by an inductively coupled plasma-optical emission spectroscopy (Thermo iCAP 6300). XRD spectra of samples were collected on Rigatku Ultima 4 X-ray diffractometer utilizing Cu Kα radiation. Surface areas were obtained from N_2 adsorption at –196 ºC. Scanning electron microscopy (SEM, SUPRRATM 55), TEM and high-resolution TEM (HRTEM, FEI Tecnai G2 F20) investigations were performed to reveal the morphology of the materials. Scanning TEM (STEM) and EDX studies were also did on a FEI Tecnai

G2 F20 microscope with an Oxford EDX detector. The Co and Fe K-edge XAFS data were recorded on the BL11B beamline of Shanghai Synchrotron Radiation Facility at 25 ºC, operated with the electron beam energy of 2.5 GeV and the current of 200 mA. H_2–TPR and CO_2/H_2/CO–TPD measurements were performed on a Micromeritics ChemiSorb 2920. The H_2/CO and CO_2 signals were detected by a thermal conductivity detector (TCD) and mass spectrometer (OmniStar GSD320 02), respectively. For H_2–TPR, the 100 mg catalyst is treated in Ar gas at 150 ºC for 1 h, and then placed in the 5%H_2/95%Ar mixture at 50 ºC. After the baseline is stabilized, the temperature was programmed to rise to 750 ºC. For CO_2−TPD, after pretreatment of the material, a CO_2 flow was continued at 50 ºC for 1.5 h. Switch the Ar gas to purge until the CO_2 signal (m/z = 44) is stable at 50 ºC, and then heat up to 500 ºC. For H_2/CO–TPD, firstly, the material was reduced with H_2 at 400 ºC for 6 h and then flushed with inert gas for 1 h at 400 ºC and cooled to 50 ºC. A pure H_2 or CO flow was continued for 1 h at 50 ºC and the desorption of H_2 or CO was conducted from 50 to 750 ºC under pure Ar. The X-Ray absorption spectra (XAS) were recorded at the BL11B beamline of Shanghai Synchrotron Radiation Facility (SSRF). The beam current of the storage ring was 220 mA in a top-up mode. The incident photons were monochromatized by a Si(111) double-crystal monochromator, with an energy resolution $\Delta E/E \sim 1.4 \times 10^{-4}$. The rejection of higher harmonics was achieved by a pair of Cr-coated mirrors at 4 mrad. The spot size at the sample was ~200 μm × 250 μm (H × V). The XAS spectra were recorded in the transmission mode. The *in situ* DRIFTS were collected by a Nicolet 6700 infrared spectrometer equipped with a cylindrical cavity cell and MCT detector. Before DRIFTS analyses, catalysts (30 mg) undergone the same reduction pretreatment in the cell as the H_2/CO–TPD process, which were then cooled down to the target temperatures under Ar and the corresponding background spectra at different temperatures (50, 100, 150, 200 and 240 ºC) were collected for subsequent DRIFTS

analyses. After that, the flow of Ar was switched to pure CO_2 at 50 ºC, and IR spectra were recorded when increased severe specific temperatures (50−240 ºC) for 10 mins. After CO_2 flow at 240 ºC for 40 min, the H_2 stream was introduced into the cylindrical cavity cell. IR spectra were recorded for CO_2 hydrogenation at 240 ºC and specific times in the range of 1−60 min. XPS experiments were performed in a ThermoFischer photoelectron spectrometer (ESCALAB 250Xi) equipped with non-monochromatic X-ray Irradiation Mg Kα (hv = 1253.6 eV). The device was also equipped with a 180° double focusing hemispherical analyzer with a six-channel detector. The Mg Kα source was chosen since under Al Kα irradiation there is strong overlapping of Co 2p photoemission spectrum with Fe LMM Auger peaks and overlapping of Fe 2p spectrum with Co LMM Auger peaks which makes the spectra analysis very difficult. The C 1s peak located at 284.9 eV associated with adventitious carbon was used to calibrate all XPS peak spectra. *In situ* reduction and subsequent reaction over the catalyst were performed in an ultra-high vacuum connected Fermi Model HPGC 300 high pressure gas cell. Typically, the calcined CoFe-0.81Na catalyst was first reduced in 0.1 MPa of H_2 at 400 ºC for 3 h. *In situ* CO_2 hydrogenation reaction was performed in 0.8 MPa CO_2 and H_2 for 5 h at 200 ºC or 240 ºC. XPS spectra were recorded after cooling of the sample in the correspond flow, pumping down and transfer to the analysis chamber of the spectrometer.

Catalytic evaluation. The mixture of catalyst (0.5 g) and the same volume of quartz sand was filled into a fixed bed reactor. Prior to reaction, the pure H_2 (0.5 MPa) was used to reduce the catalyst at 400 ºC for 6 h. Then, when the center temperature of catalyst bed was cooled down to target temperatures, the feed gas ($H_2/CO_2/N_2$) was introduced into the stainless-steel reactor. An online gas chromatograph equipped with a TCD and a hydrogen flam ionization detector (Agilent GC 7890A) was utilized to analyze the CO_2 hydrogenation products. The conversion of CO_2 and the selectivity of CO were

calculated using an internal normalization method. Hydrocarbon distributions are determined based on total carbon moles. The carbon balance was determined to be in the range of 96~104%. The evaluation data after running for 48 h was employed in this paper.

DFT calculations. DFT calculations were performed with the VASP program using the PBE functional with spin polarization. The projector-augmented wave (PAW) method was used with an energy cutoff of 400 eV. CoO, Co, and CoFe phases were modeled by the p(2×2) supercell with 4 atomic layers (ALs) for Co(100), the p(2×3) supercell with 4 ALs for Co(10-11), and the p(3×2) supercell with 5 ALs for Co/Fe(100), respectively, using the k-point grids of (7×7×1), (5×3×1), and (3×3×1). Models for the Na-promoted Co and CoFe phases are similar to those adopted in the literature.[1] Atoms in the top three atomic layers along with those in the adsorbate were fully relaxed with a force convergence of 0.05 eV/Å. Adjacent slabs were separated by a 20 Å vacuum region to avoid possible interaction between neighboring slabs. The transition state with four or more images was found using the climbing image nudged elastic band (CI-NEB) approach with four or more images. Charge density difference analysis was performed with VESTA by calculating the charge difference before and after the adsorption of an adsorbate.

Table S1. Metal compositions and textural properties of CoFe-*x*Na, Co-*x*Na and Fe-*x*Na catalysts.

Catalysts	Metal content (wt %)			Molar ratio	BET specific surface area ($m^2\ g^{-1}$)	BJH pore volume ($cm^3\ g^{-1}$)	Pore diameter (nm)
	Co	Fe	Na	Co/Fe			
$CoFe/Al_2O_3$-1.09Na	42.0	20.1	1.09	1.98	97	0.40	16.6
CoFe-0.82Na-U	47.1	22.5	0.83	1.98	66	0.15	12.1
CoFe-3.54 Na	45.1	22.2	3.54	1.93	54	0.30	22.1
CoFe-0.81Na	47.0	22.9	0.81	1.94	69	0.30	17.4
CoFe-0.23 Na	47.5	23.0	0.23	1.96	75	0.38	20.1
CoFe	47.2	23.4	0.01	1.91	585	0.22	14.9
Co-0.63 Na	70.5	−	0.63	−	50	0.23	18.6
Co	71.0	−	0.02	−	28	0.17	24.3
Fe-0.67 Na	−	69.7	0.67	−			
Fe	−	72.4	0.01	−			

CoFe without Na were obtained by washing precursors 50 times, which destroyed the LDH structure as shown by the much lower crystallinity of CoFe precursors (Figure S5A) and results in the decrease of specific surface areas. However, excessive amount of residual Na can block the channel of CoFe-3.54Na, which also decreases the BET surface area.

Table S2. Comparison of the catalytic performance of various catalysts for the CO_2 hydrogenation to C_8–C_{16} hydrocarbons.

Catalyst	Active site	P (MPa)	T (°C)	WHSV (mL g_{cat}^{-1} h^{-1})	H_2/CO_2	CO_2 Conv. (%)	CO Select. (%)	C_8–C_{16} Select. in HC (%)	C_8–C_{16} Yield [a]	Ref.
Fe-Mn-K	χ-Fe_5C_2	1	300	2400	3	38.2	5.6	47.8	65	[2]
Fe-Cu	χ-Fe_5C_2	1	300	1800	3	16.7	31.4	~37	12	[3]
Fe-Zn	χ-Fe_5C_2	1	340	1800 (7.69%N_2)	3	34	11.7	~49	35	[4]
FeK/Co-NC	Fe-Co mixed carbide	2.5	300	2000 (10%Ar)	3	54.6	~3	~30	40	[5]
CoFe-0.81Na	CoFe alloy	3	240	5500 (3%N_2)	3	10.2	5.2	63.5	51	This work

[a] Unit in mg g_{cat}^{-1} h^{-1}

Table S3. The catalytic performance of various catalysts in the CO_2 hydrogenation reaction.

Entry	Catalysts	Conv. (%)	CO Sel. (%)	Hydrocarbon distribution (C mol%)			
				CH_4	C_2–C_4	C_5–C_7	C_{8+}
1	CoFe-0.82Na-U	11.0	5.4	22.7	9.1	8.3	59.9
2	CoFe/Al_2O_3-1.09Na	37.2	0.3	33.9	16.5	9.9	39.7
3	Fe-0.67Na	5.0	59.2	17.2	23.2	15.5	44.1
4	Fe	9.1	4.5	50.9	41.1	1.2	6.8

Standard reaction conditions: $H_2/CO_2/N_2$ = 73/24/3, T = 240 °C, GHSV = 5500 mL·g^{-1}·h^{-1}, P = 3 MPa. The data is collected after 48 h time on stream.

The space-time yield of C_8–C_{16} over CoFe-0.81Na was found to be comparable to those of catalysts with carbides as the active phases at the much lower reaction temperature, though the CO_2 conversion is also lower (Table S2). In general, reducing the metal nanoparticle sizes or enhancing the metal dispersion can improve metal utilization efficiency and lead to higher activity for CO_2 hydrogenation.[6-9] To further increase the catalytic activity, we synthesized small CoFe-LDH nanosheets by using the reported ultrasonic method,[10] and obtaining CoFe-0.82Na-U after calcination. As shown in Table S3, the CoFe-0.82Na-U catalyst exhibits a similar catalytic performance to CoFe-0.81Na with a slightly higher CO_2 conversion. It is generally accepted that the introduction of supports such as Al_2O_3 can enhance the dispersion of metal nanoparticles and reduce their particle sizes. We also prepared CoFe/Al_2O_3-1.09Na with the Co/Fe molar ratio of 1.98 by using CoFeAl-LDH as the precursor. Compared with CoFe-0.81Na, the CO_2 conversion over CoFe/Al_2O_3-1.09Na amounts to 37.2% (Table S3, Entry 2), which is about 3.7-fold higher than that over CoFe-0.81Na, although C_{8+} selectivity decreases to 39.7% with a much higher CH_4 selectivity (33.9% vs 17.8%).

Table S4. Co K-edge EXAFS fitting results for CoFe-0.81Na catalysts and Co foil.[a]

Sample	Pair	CN	R (Å)	σ^2 (x 10^3)	ΔE_o (eV)
Co foil	Co−Co	12	2.50	6.94	6.0
CoFe-0.81Na-calcined	Co−O	1.2	1.90	3.09	2.55
	Co−Co	4.1	2.08	2.23	25.6
CoFe-0.81Na-reduced	Co−Fe	2.2	2.49	0.55	65.6
	Co−Co	2.1	2.47	0.53	20.2
CoFe-0.81Na-spent	Co−Fe	2.4	2.48	0.56	67.8
	Co−Co	2.3	2.47	0.53	20.8

[a] CN, coordination number; R, interatomic distance; σ^2, disorder parameter; ΔE_o, energy shift. All the fitting analysis were performed in the R space, $\Delta R = 1.0-3.5$ and $\Delta K = 2.0-11.2$.

Table S5. Fe K-edge EXAFS fitting results for CoFe-0.81Na catalysts and Fe foil.

Sample	Pair	CN	R (Å)	σ^2 (x 10^3)	ΔE_o (eV)
Fe foil	Fe−Fe	8	2.48	6.20	6.5
CoFe-0.81Na-calcined	Fe−O	0.5	1.96	1.04	2.96
	Fe−Fe	5.6	2.68	7.37	26.9
CoFe-0.81Na-reduced	Fe−Co	2.0	2.51	0.56	31.2
	Fe−Fe	2.3	2.46	1.66	59.4
CoFe-0.81Na-spent	Fe−Co	2.2	2.51	0.35	22.8
	Fe−Fe	2.5	2.49	1.65	62.4

Table S6. Energy barriers (E_a) and reaction energies (Δ_rE) in eV for CH_x (x = 1, 2) hydrogenation and coupling reactions on the Co(10-11) and CoFe(110) surfaces. The numbers in the parentheses are for the Na-promoted Co(10-11) and CoFe(110) surfaces.

Surface elementary steps	Co(10-11)		CoFe(110)	
	E_a	Δ_rE	E_a	Δ_rE
$CH^* + H^* \rightarrow CH_2 + *$	0.62 (0.64)	0.55 (0.57)	0.42 (0.62)	0.26 (0.40)
$CH_2^* + H^* \rightarrow CH_3^* + *$	0.53 (0.51)	−0.14 (−0.05)	0.57 (0.66)	−0.10 (0.15)
$CH^* + CH_2^* \rightarrow CHCH_2^* + *$	0.17 (0.31)	−0.25 (−0.15)	0.61 (0.86)	−0.01 (−0.07)
$CH_2^* + CH_2^* \rightarrow C_2H_4^* + *$	0.38 (0.25 [a])	−0.40 (−0.35)	0.51 (0.62)	−0.38 (−0.54)

[a] Estimated from the BEP relationship.

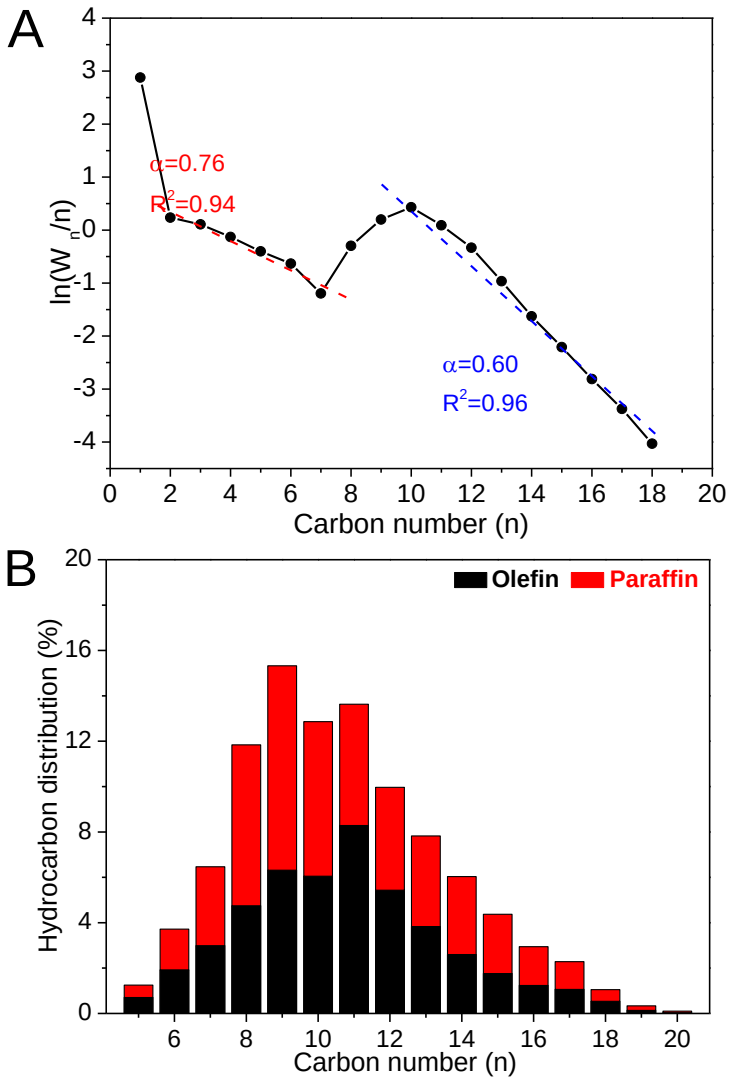

Figure S1. Hydrocarbon distribution for CO_2/CO hydrogenation (A) ASF plot and α values over the CoFe-0.81Na catalyst under the reaction condition shown in Table S3. W_n is the weight fraction of a hydrocarbon with *n* carbon atoms. (B) Hydrocarbon distribution of the liquid products of CO hydrogenation over the CoFe-0.81Na catalyst at $H_2/CO/N_2 = 73/24/3$, T = 240 ºC, GHSV = 5500 $mL \cdot g^{-1} \cdot h^{-1}$, P= 3 MPa.

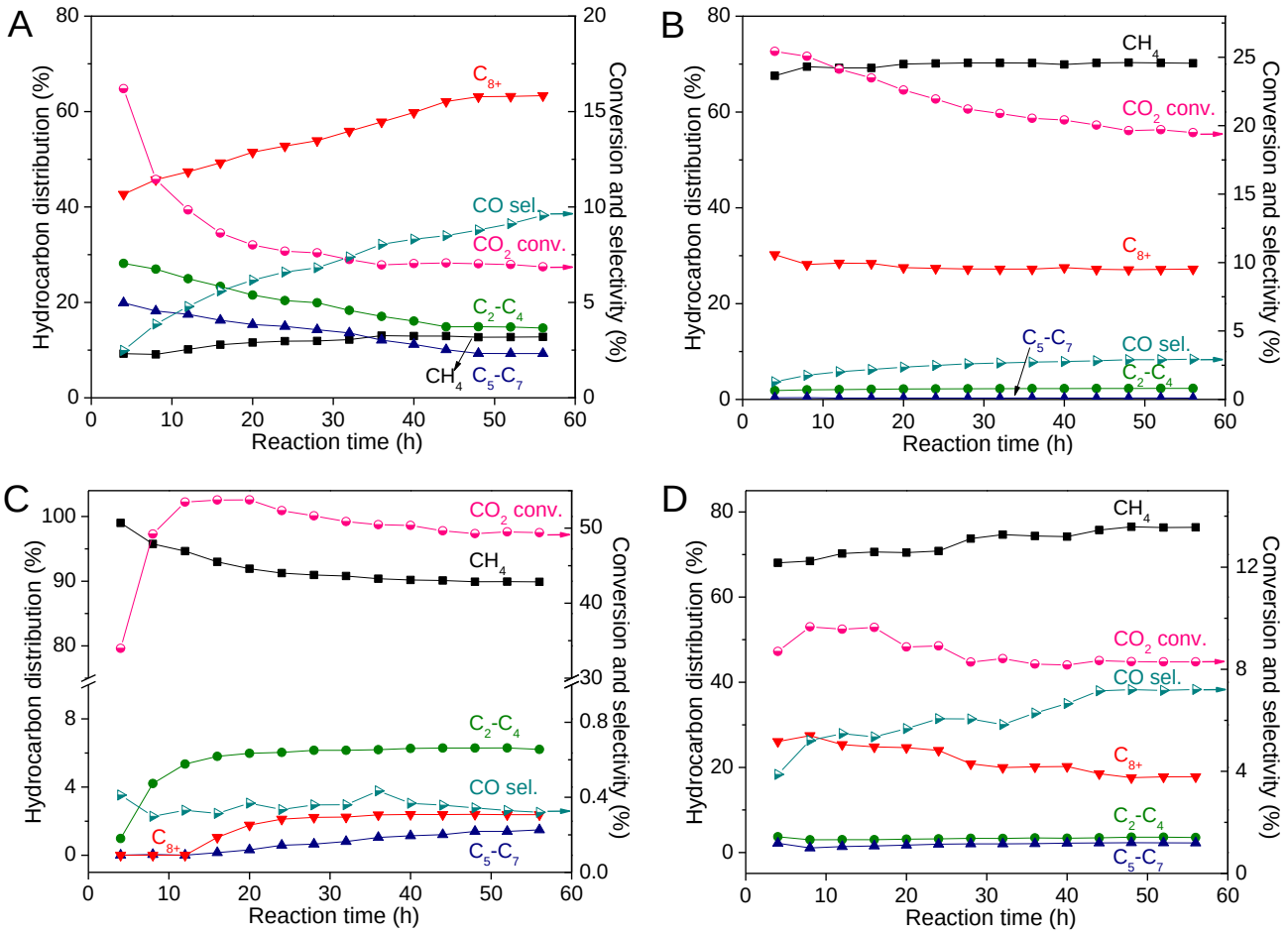

Figure S2. Catalytic stability (A−D) CO_2 hydrogenation performance of (A) CoFe-3.54Na, (B) CoFe, (C) Co and (D) Co-0.63Na catalysts with time-on-stream under standard reaction conditions.

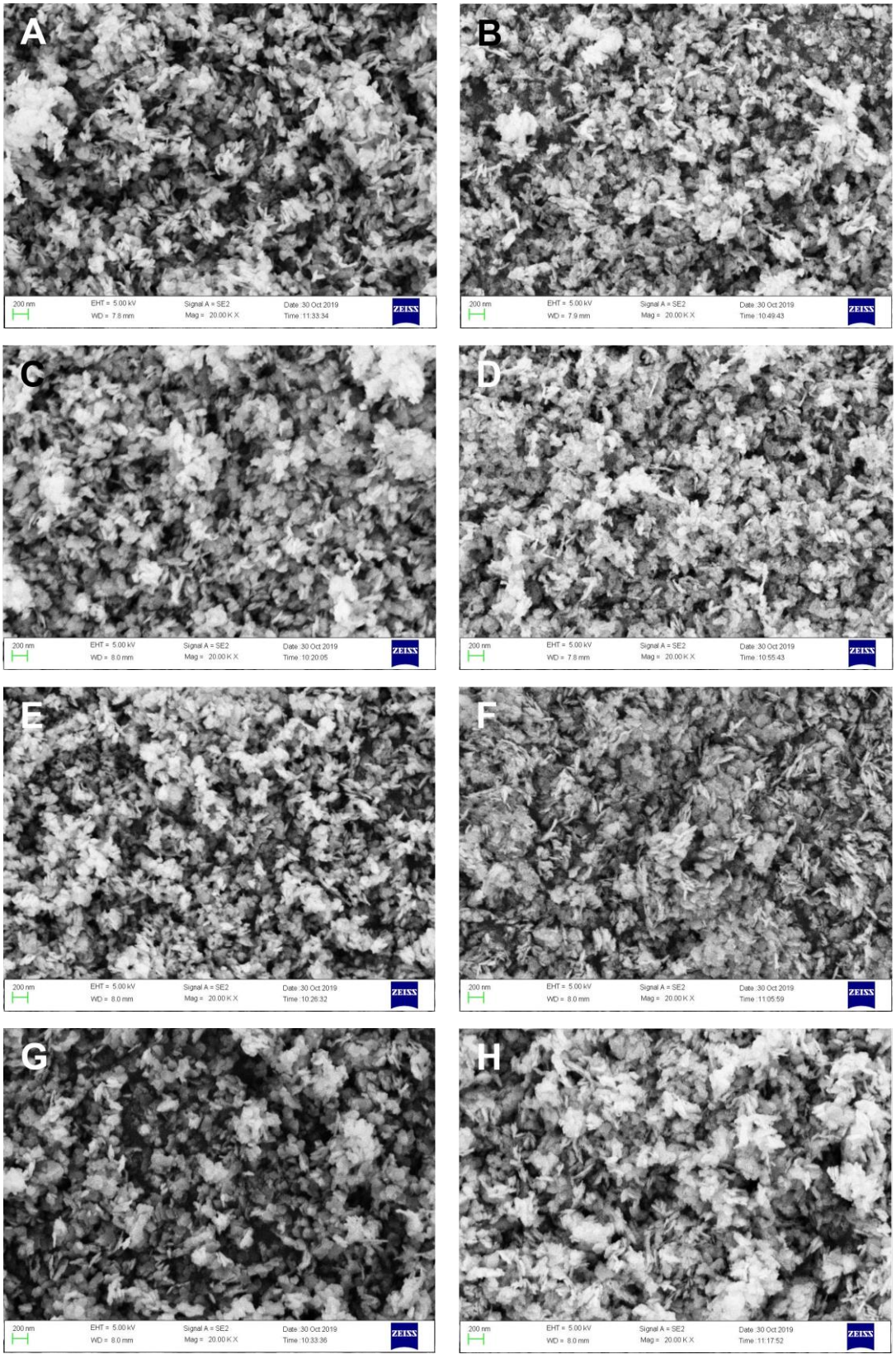

Figure S3. Morphology of uncalcined precursors and corresponding calcined samples SEM images of (A) CoFe, (C) CoFe-0.23Na, (E) CoFe-0.81Na and (G) CoFe-3.54Na precursors, as well as calcined (B) CoFe, (D) CoFe-0.23Na, (F) CoFe-0.81Na and (H) CoFe-3.54Na catalysts.

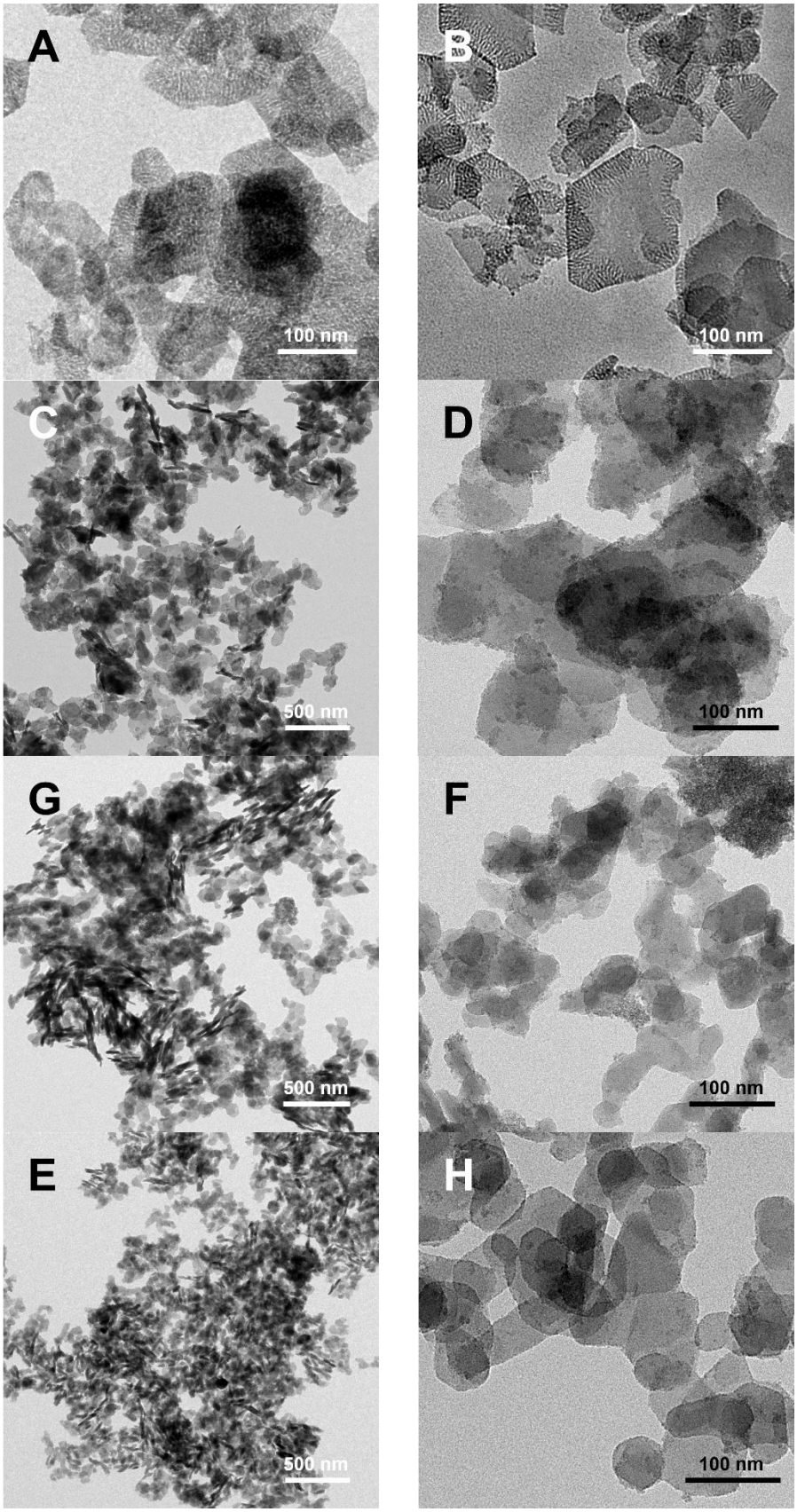

Figure S4. TEM images of (A) CoFe, (B) CoFe-0.81Na, (C and D) CoFe-3.54Na, (E and F) CoFe-0.82Na-U and (G and H) CoFe/Al_2O_3-1.09Na uncalcined precursors.

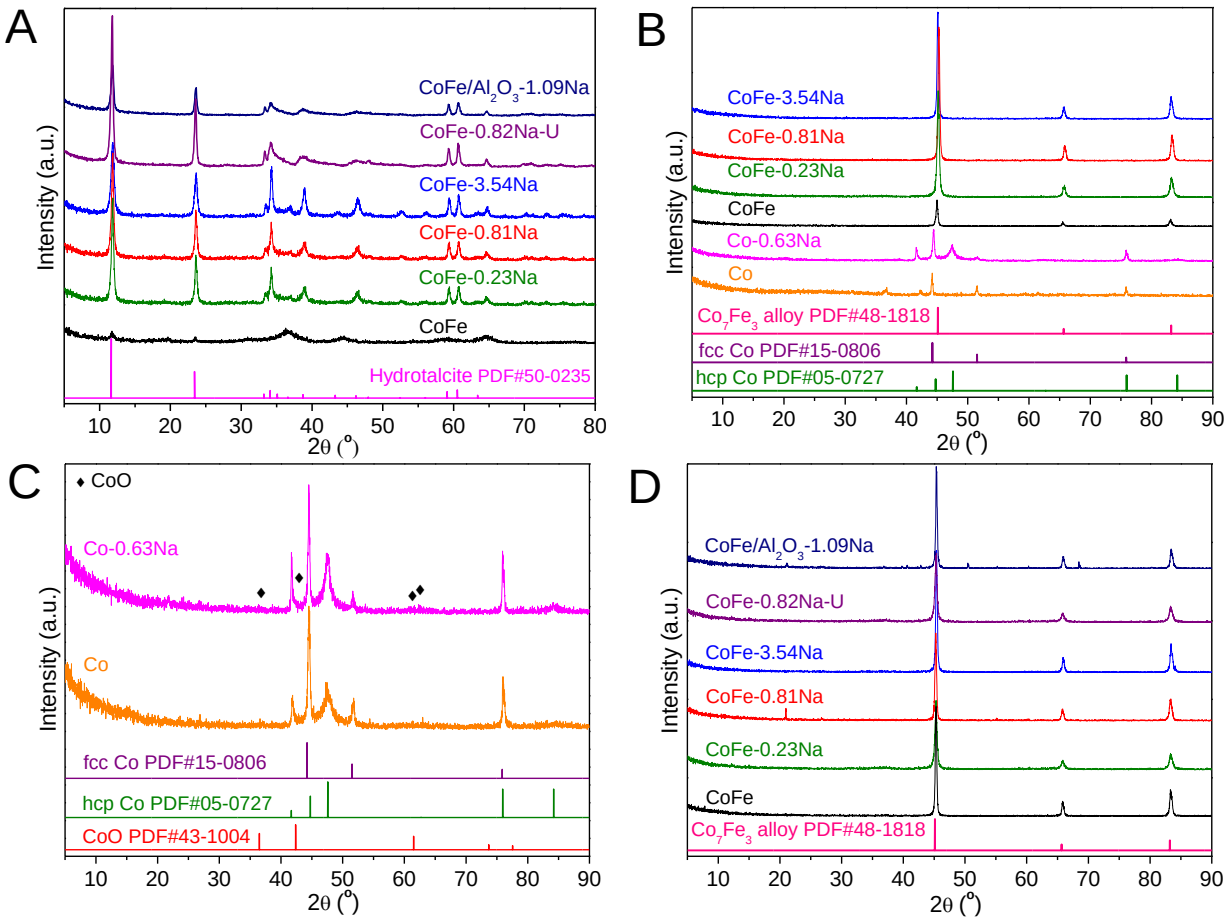

Figure S5. XRD patterns of (A) uncalcined precursors of various catalysts, as well as corresponding (B) reduced and (C and D) used samples.

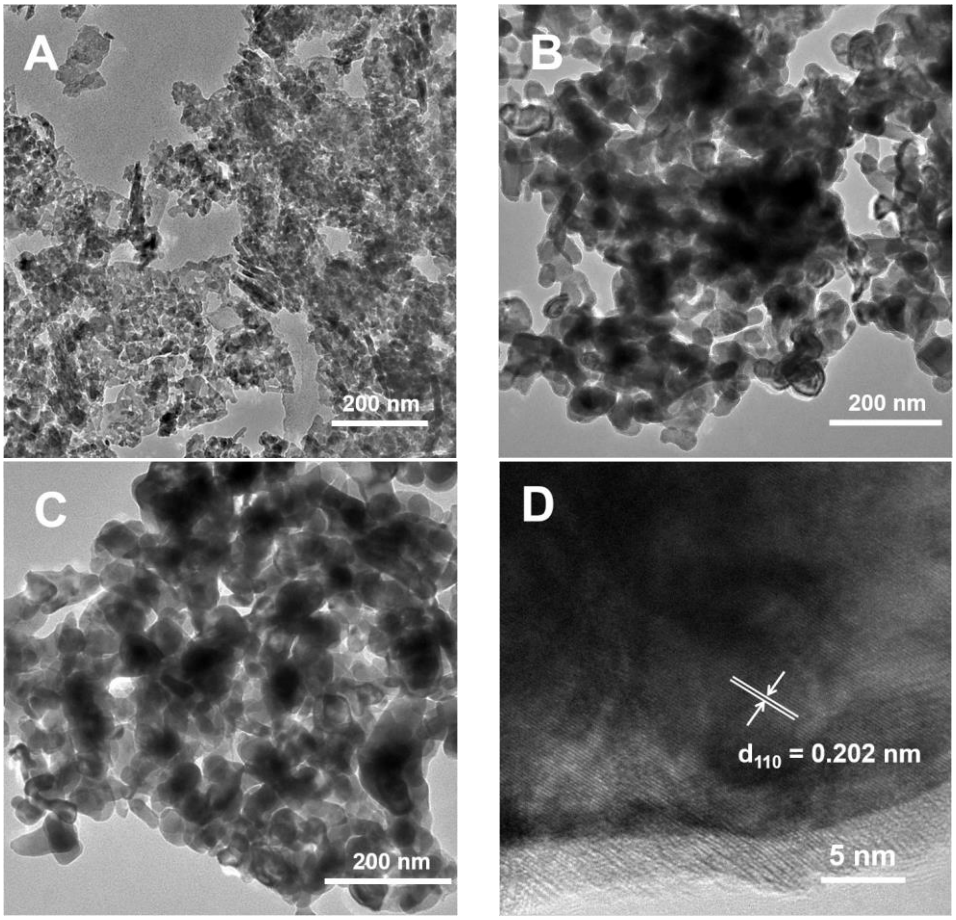

Figure S6. (A−E) TEM images of (A) calcined, (B) reduced and (C) used CoFe-0.81Na. (D) HRTEM images of used CoFe-0.81Na after CO_2 hydrogenation reaction.

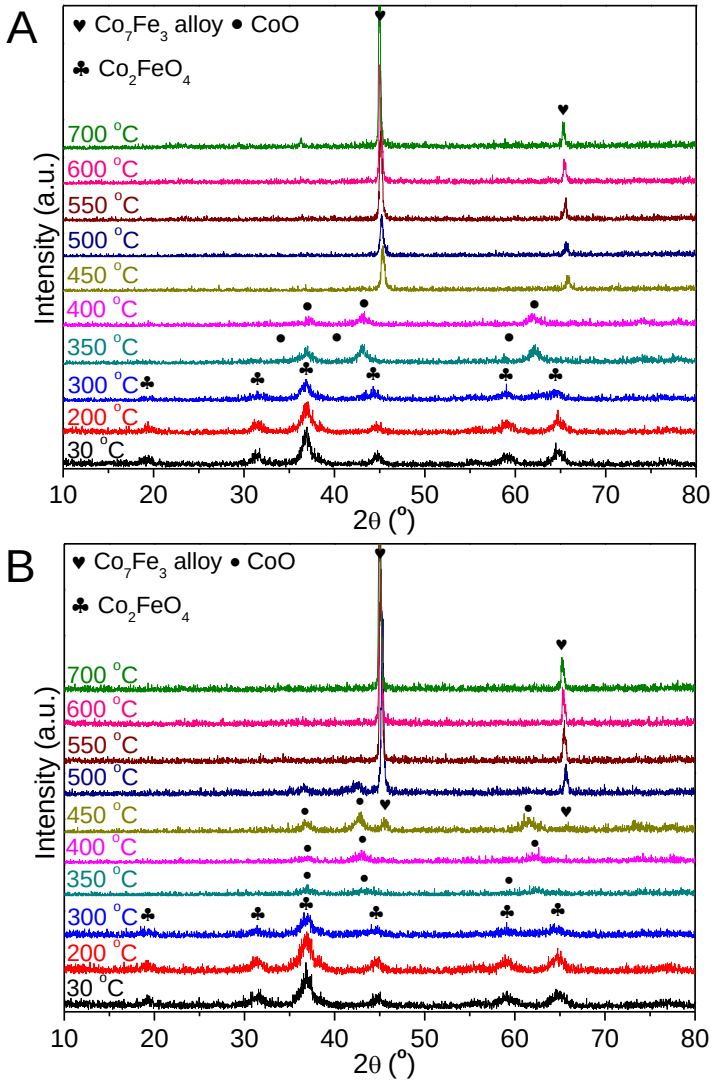

Figure S7. *In situ* XRD patterns of (**a**) CoFe-0.81Na and (**b**) CoFe-3.54Na obtained in 5% H_2/Ar with the increase of the temperature from 30 to 700 °C.

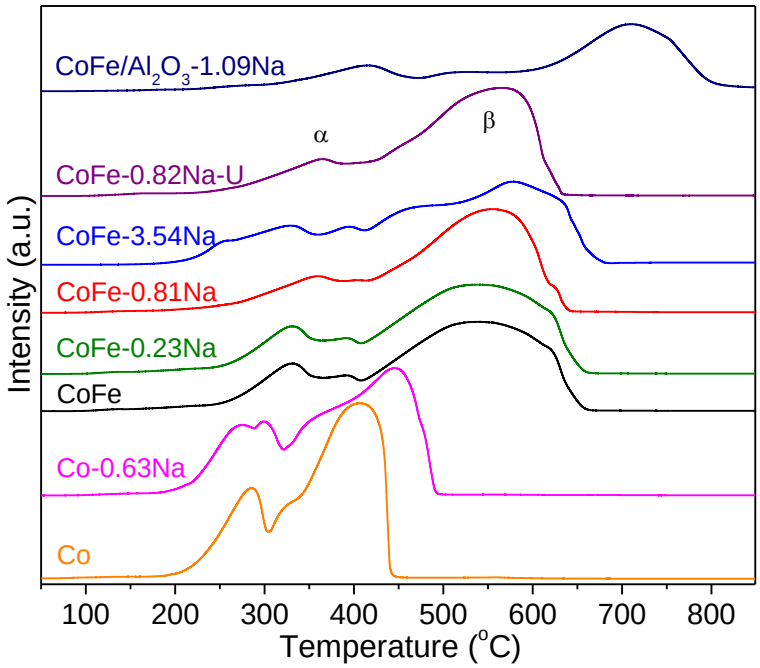

Figure S8. H_2−TPR profiles of various calcined samples.

From the H_2–TPR profiles (Figure S8), the high-temperature peaks (β peak) shift from around 560 °C for CoFe-*x*Na and CoFe-0.82Na-U to 716 °C for CoFe/Al_2O_3-1.09Na, suggesting that the introduction of the Al_2O_3 support remarkably decreases the reducibility of CoFe/Al_2O_3-1.09Na.

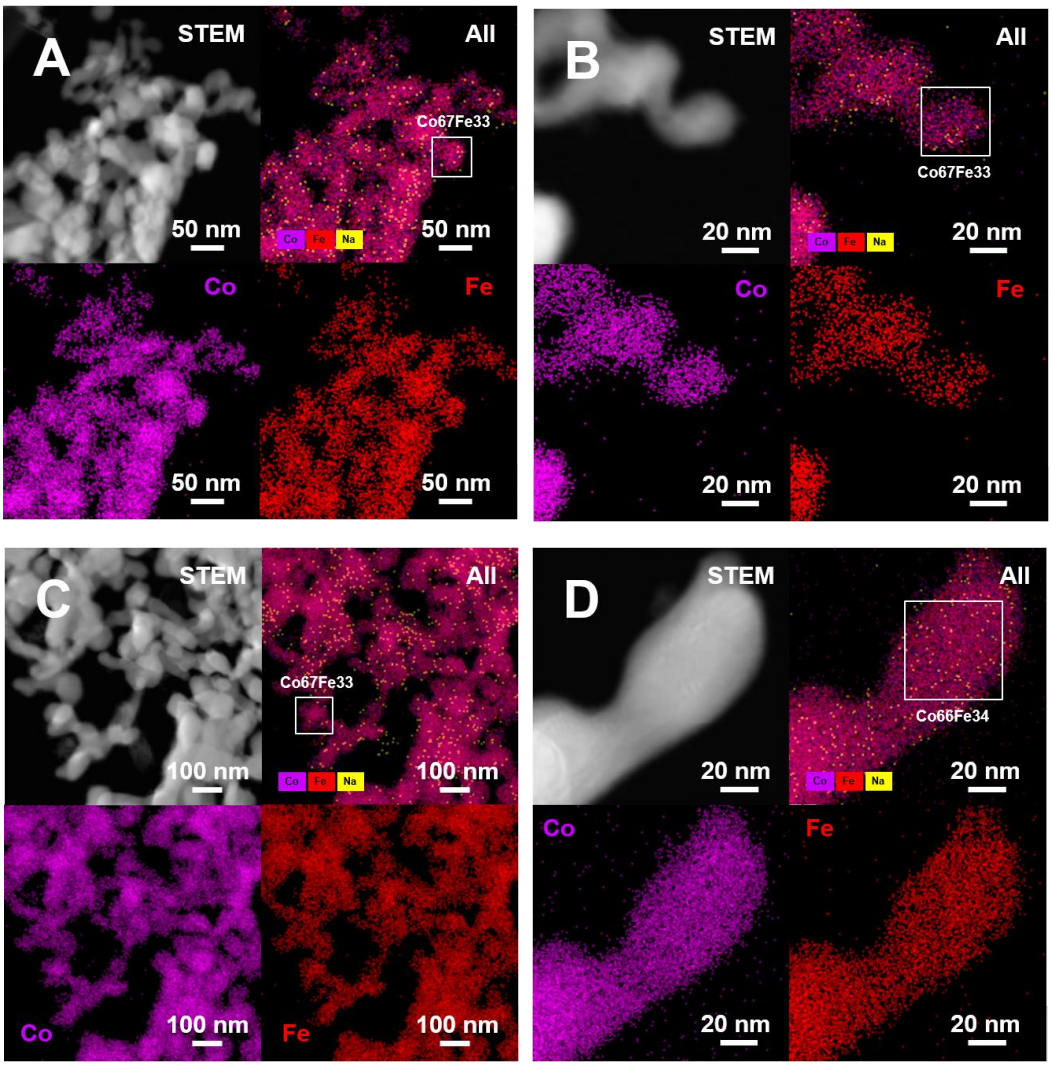

Figure S9. STEM-EDX images of reduced (A and B) CoFe-0.81Na and (C and D) CoFe-3.54Na catalysts. Co (magenta), Fe (red), Na (yellow).

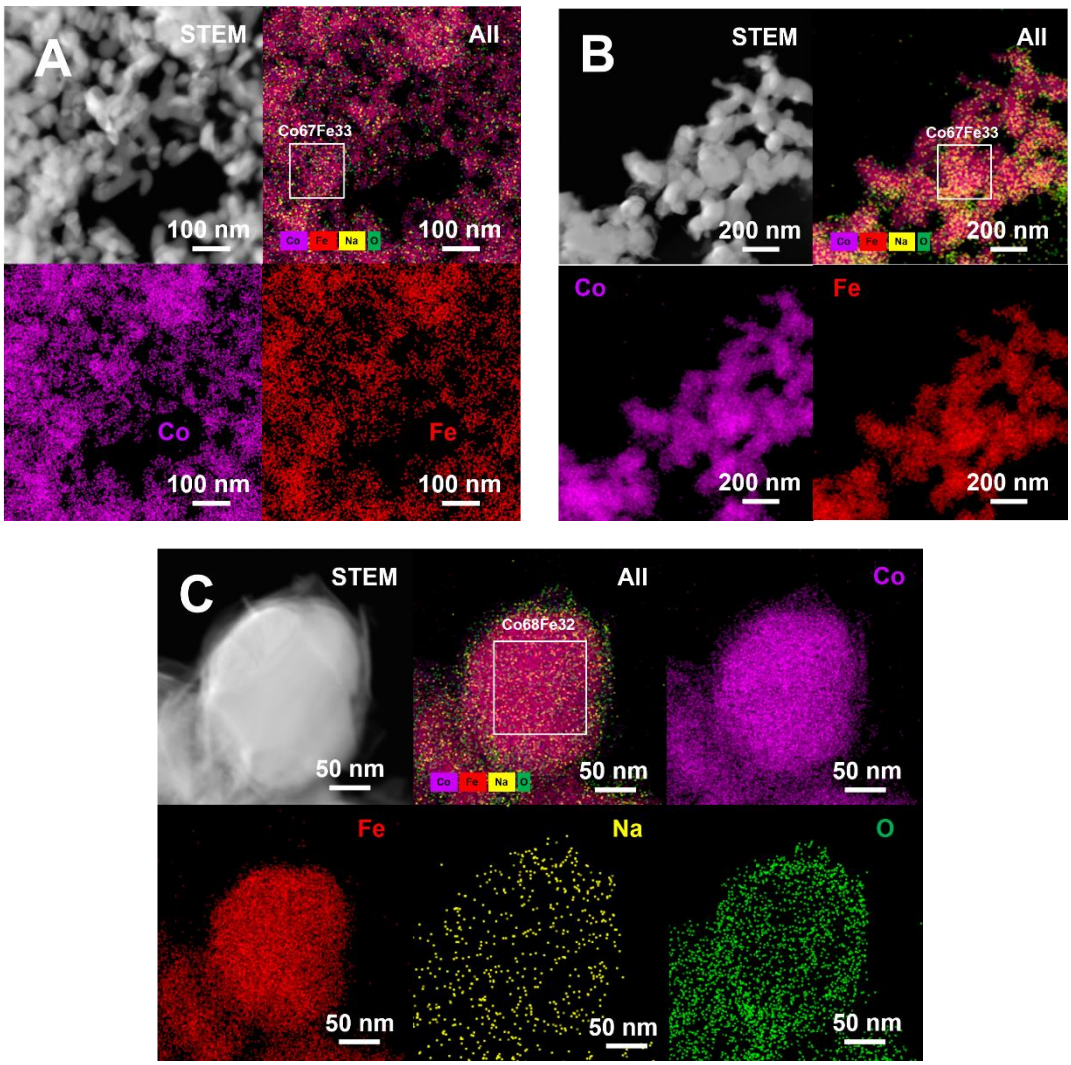

Figure S10. STEM-EDX images of spent (A) CoFe-0.81Na and (B and C) CoFe-3.54Na catalysts. Co (magenta), Fe (red), Na (yellow), O (green).

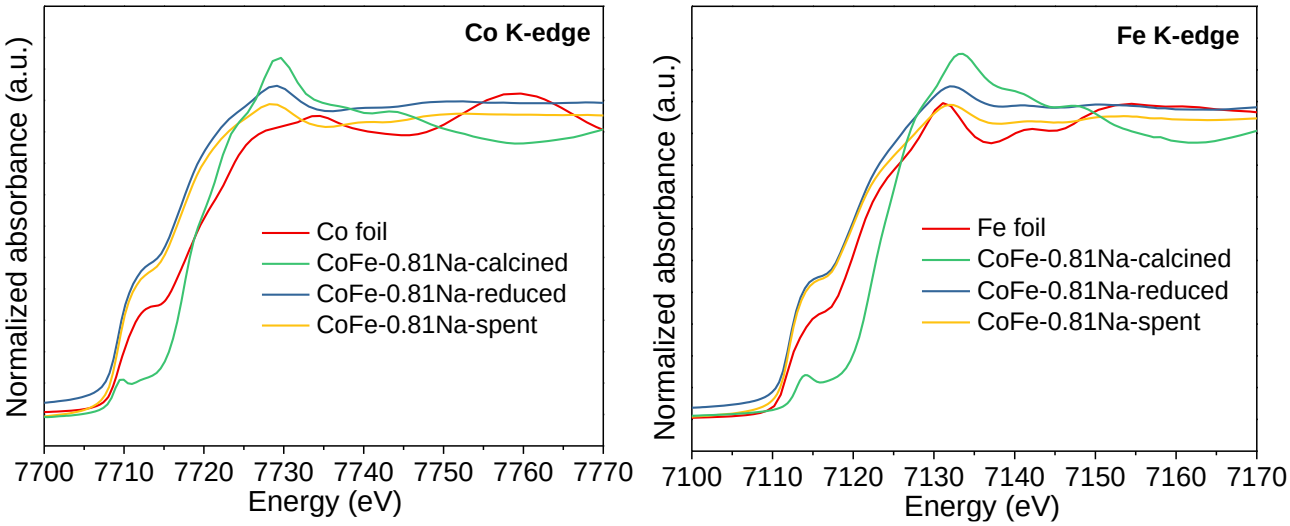

Figure S11. XANES spectra of the calcined, reduced and spent CoFe-0.81Na and reference samples at the Co and Fe K-edge.

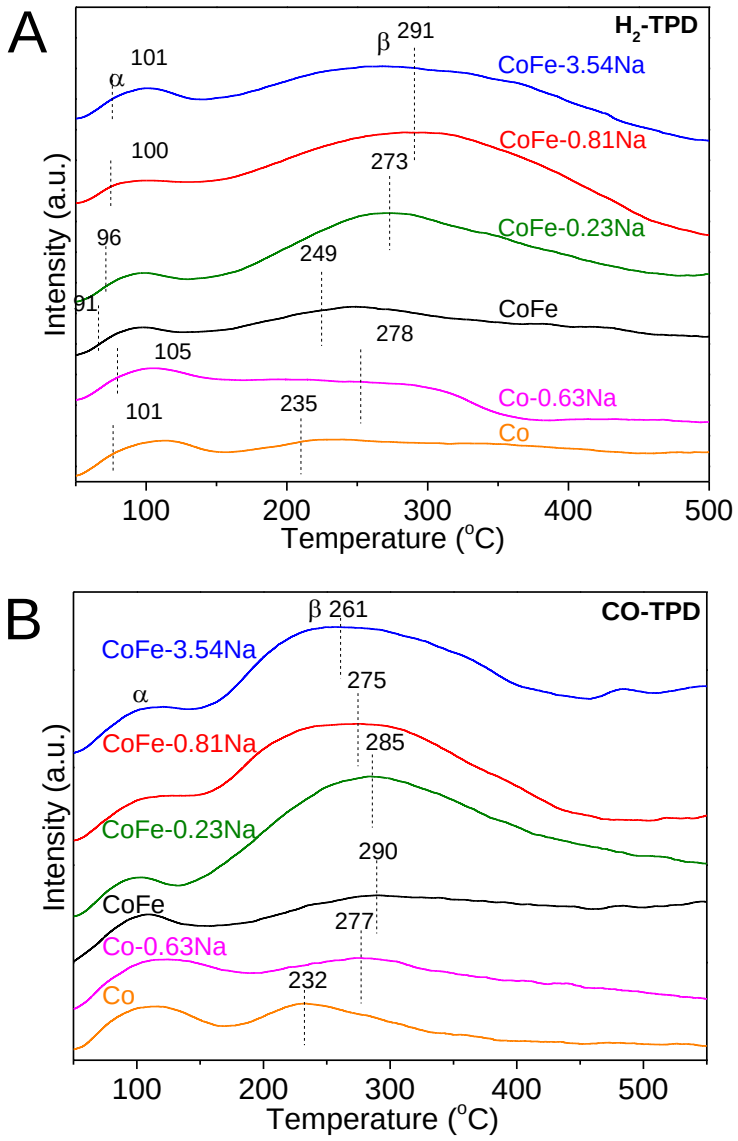

Figure S12. H_2/CO−TPD characterizations (A) H_2−TPD and (B) CO−TPD profiles over various catalysts.

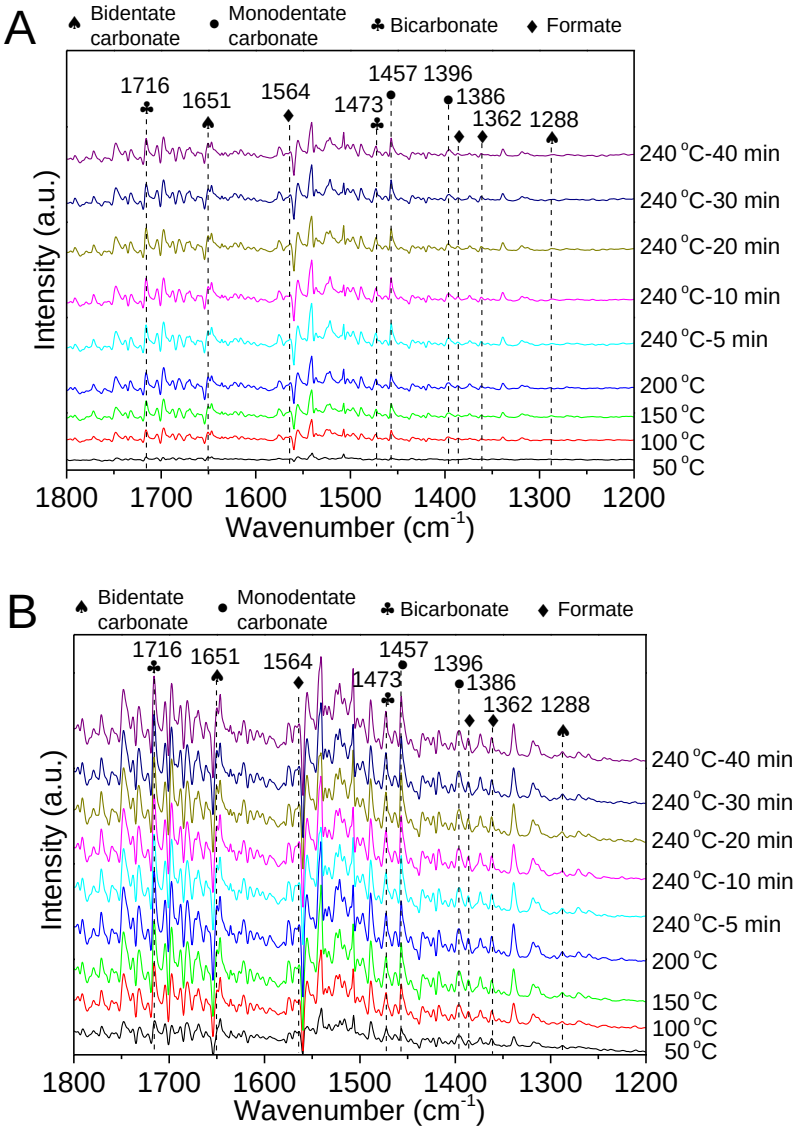

Figure S13. *In situ* DRIFTS analysis of (A) Co and (B) CoFe catalysts during CO_2 adsorption were collected at different temperature and times.

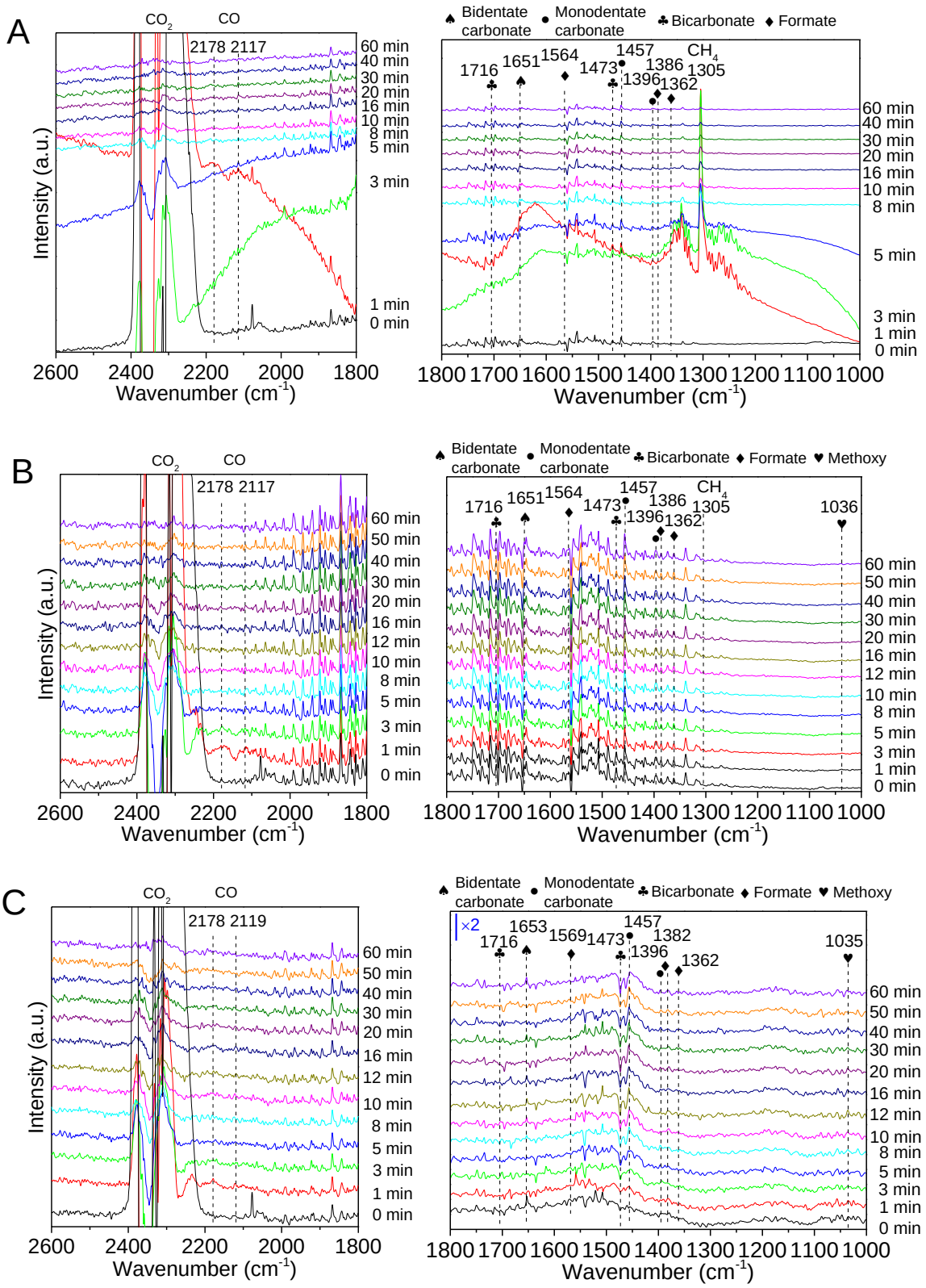

Figure S14. *In situ* DRIFTS analysis of (A) Co, (B) CoFe, and (C) CoFe-0.81Na catalysts during CO_2 hydrogenation were collected at 240 °C and different times.

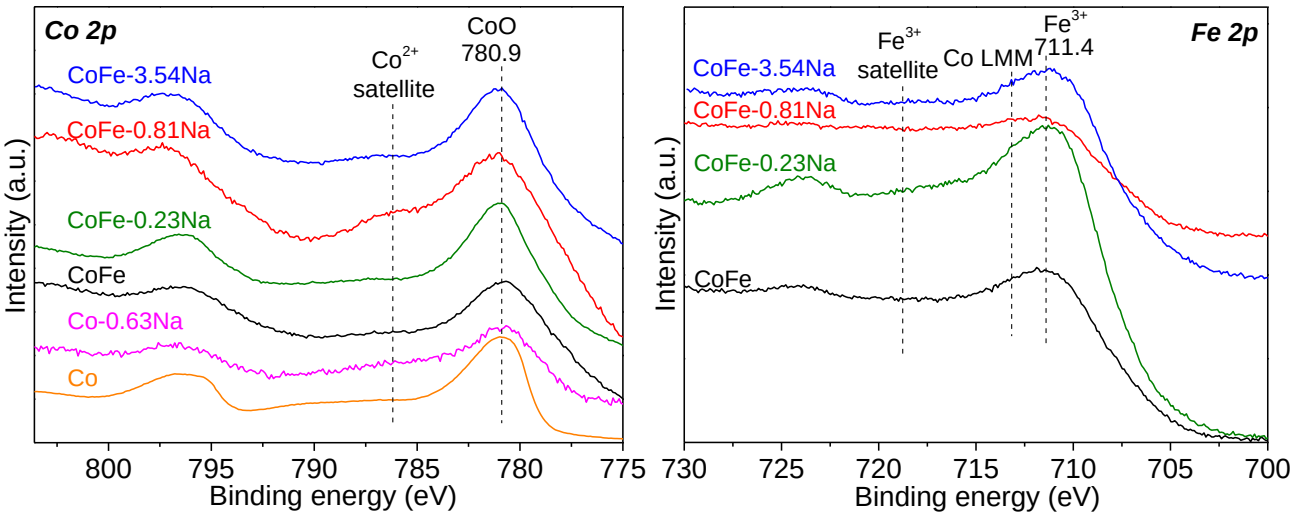

Figure S15. *Ex situ* XPS Co 2p and Fe 2p spectra of the various catalysts after CO_2 hydrogenation reaction for 48 h. The spectra are taken with Al X-ray source.

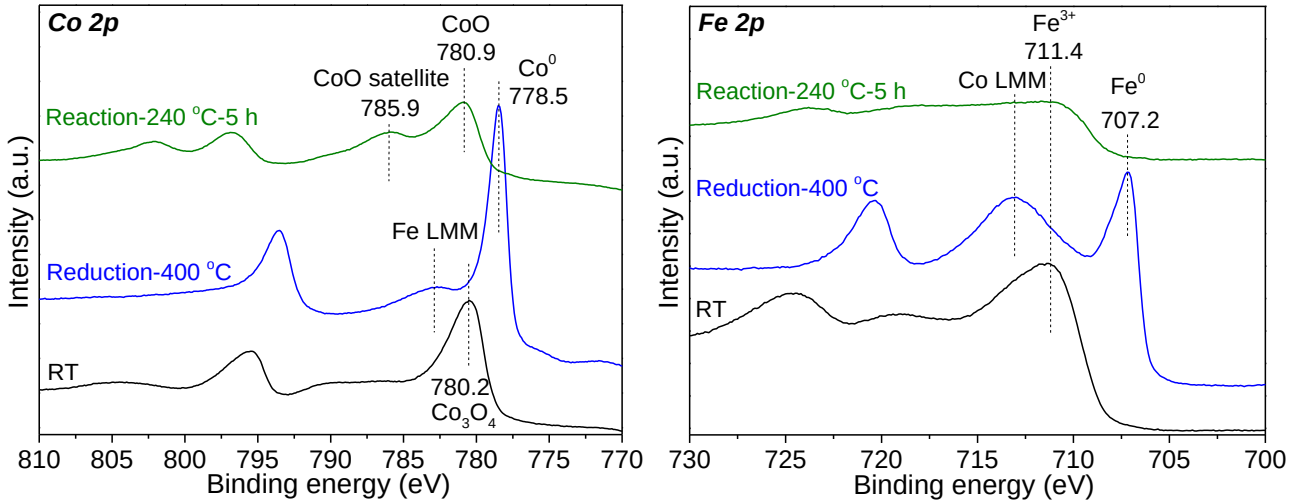

Figure S16. *In situ* XPS Co 2p and Fe 2p spectra of the fresh CoFe-0.81Na catalyst (black curves), after reduction in pure hydrogen (0.1 MPa) at 400 °C for 2 hours (blue curves), after CO_2 hydrogenation reaction at 240 °C (green curves). The spectra are taken with Al X-ray source.

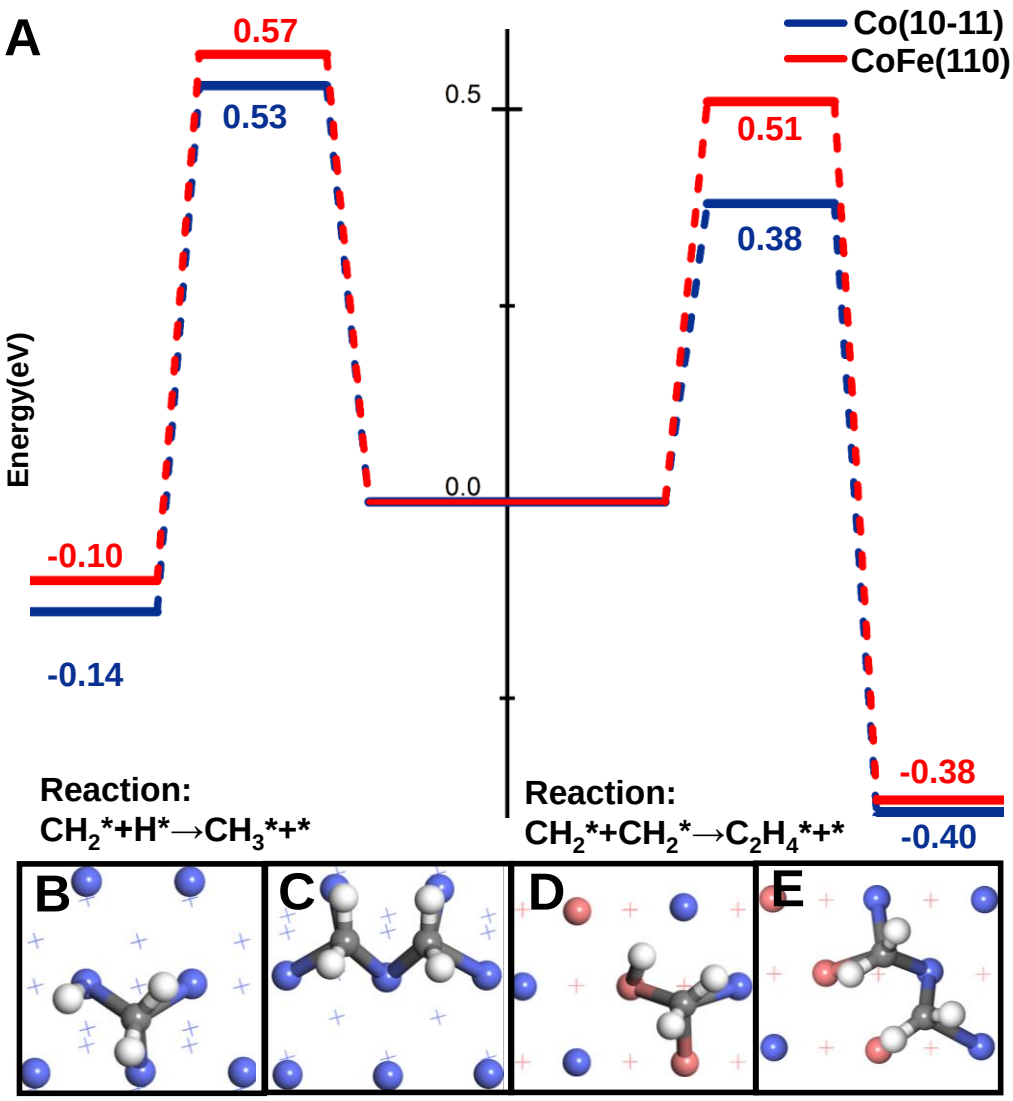

Figure S17. (A) Potential energy profiles for CH_2* hydrogenation vs. self- coupling on the Co and CoFe alloy phases modeled by the Co(10-11) and CoFe(110) slab models. (B–E) Structures of the transition states for CH_2* hydrogenation vs. self- coupling on the above two surfaces, respectively (colors of surface atoms: Co–blue, Fe–magenta, C–grey, H–white).

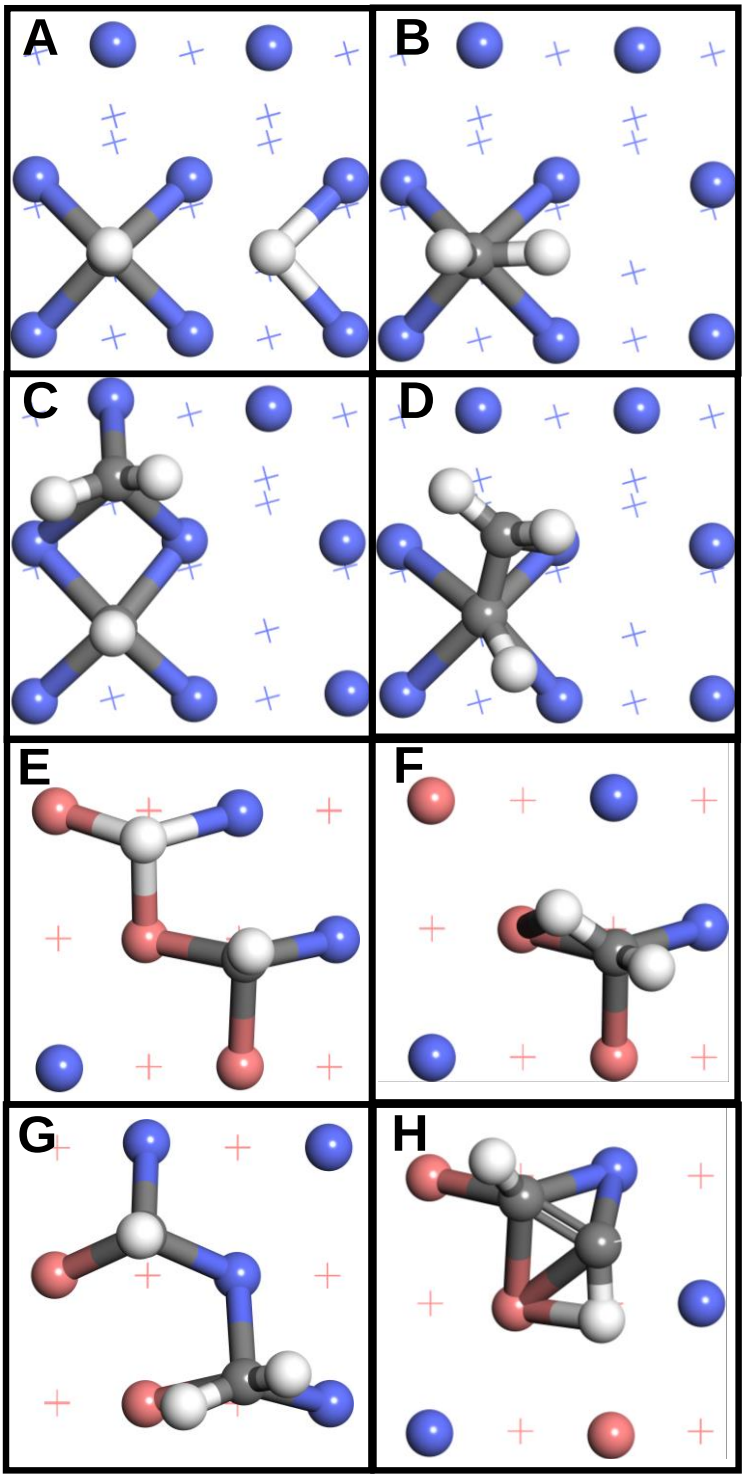

Figure S18. Structures of the initial states and final states for CH* hydrogenation vs. CH*-CH_2* coupling on the (A–D) Co(10-11) and (E–H) CoFe(110) surfaces (colors of surface atoms: Co–blue, Fe–magenta, C–grey, H–white).

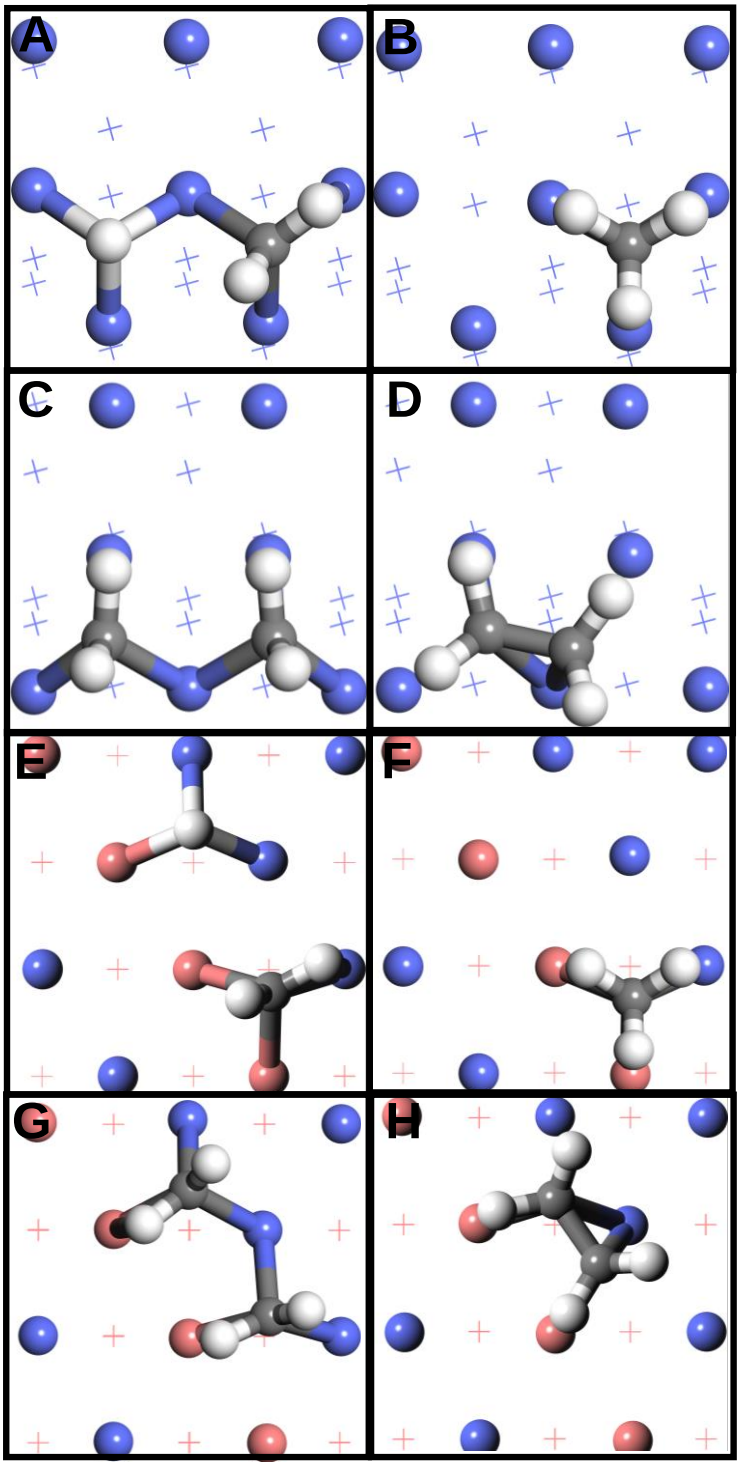

Figure S19. Structures of the initial states and final states for CH_2* hydrogenation vs. CH_2*-CH_2* coupling on the (A–D) Co(10-11) and (E–H) CoFe(110) surfaces (colors of surface atoms: Co–blue, Fe–magenta, C–grey, H–white).

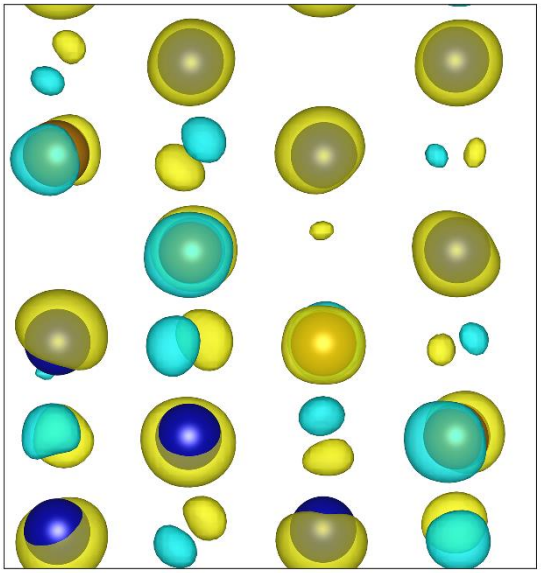

Figure S20. Isosurface of the charge density difference of the Co atoms for the CoFe(110) interface with an isovalue 0.05. Yellow indicates electron accumulation, and light blue indicates electron depletion.

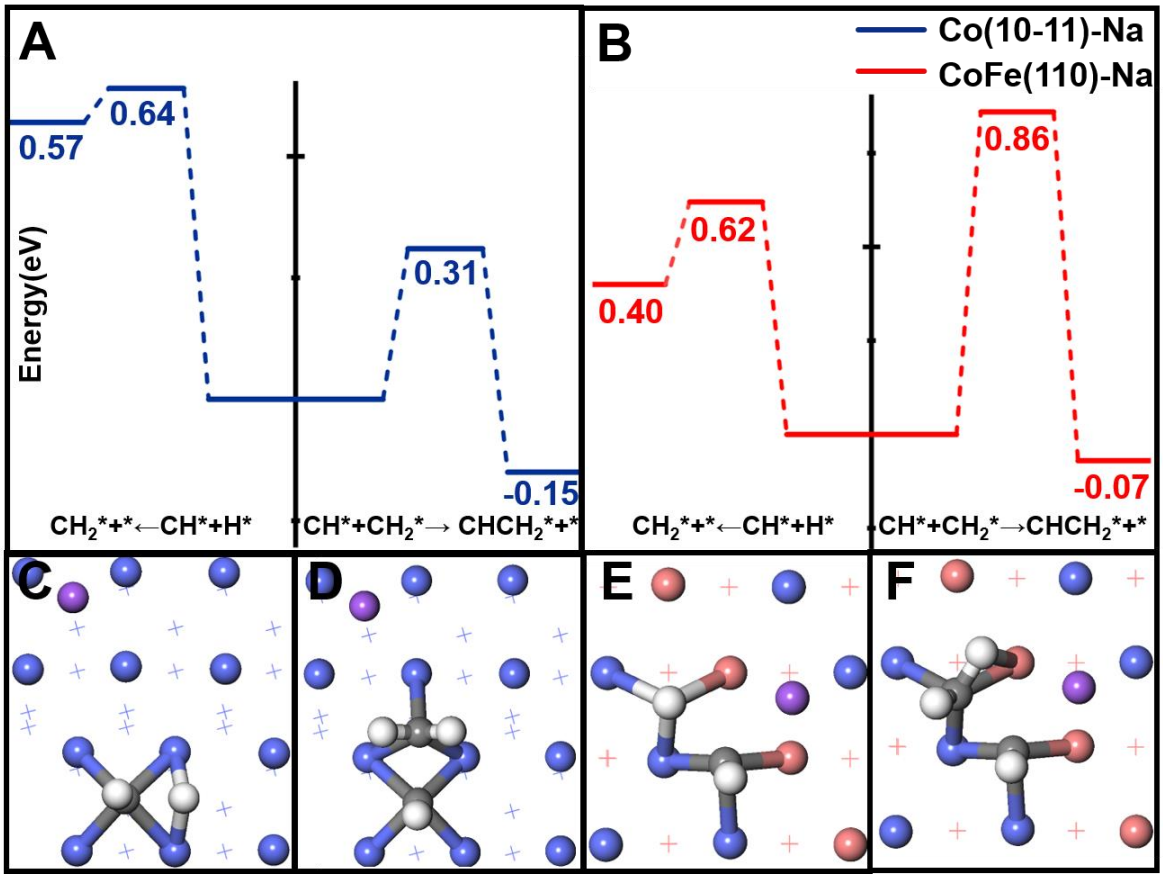

Figure S21. (A and B) Potential energy profiles for CH* hydrogenation vs. CH*+CH_2* coupling on the Na-promoted Co and CoFe alloy phases modeled by the (A) Na/Co(10-11) and (B) Na/CoFe(110) slabs. C–F Structures of the optimized transition states for (C and E) CH* hydrogenation and (D and F) CH*+CH_2* coupling on the (C and D) Na/Co(10-11) and (E and F) Na/CoFe(110) slabs, respectively (colors of surface atoms: Co–blue, Fe–magenta, Na–purple, C–grey, H–white).

Adding the Na promoter to the Co(10-11) surface leads to very similar energy barriers for CH* and CH_2* hydrogenation but a much higher barrier of 0.31 eV for CH*+CH_2* coupling by 0.14 eV and a similar estimated barrier of 0.25 eV for the self-coupling. In addition, all these reactions become thermodynamically less favorable by up to 0.1 eV. When the Na promoter is added to the CoFe(110) surface, the energy barriers of CH* and CH_2* hydrogenation and coupling all increase by 0.1 to 0.25 eV (Figure S21 and Table S6), again consistent with the observed lower CO_2 reactivity and higher CO selectivity using the Na-promoted CoFe alloy catalyst. However, the reaction energies for CH* and CH_2* hydrogenation become more endothermic by 0.15 to 0.25 eV, whereas those for their coupling are more exothermic by up to 0.16 eV.

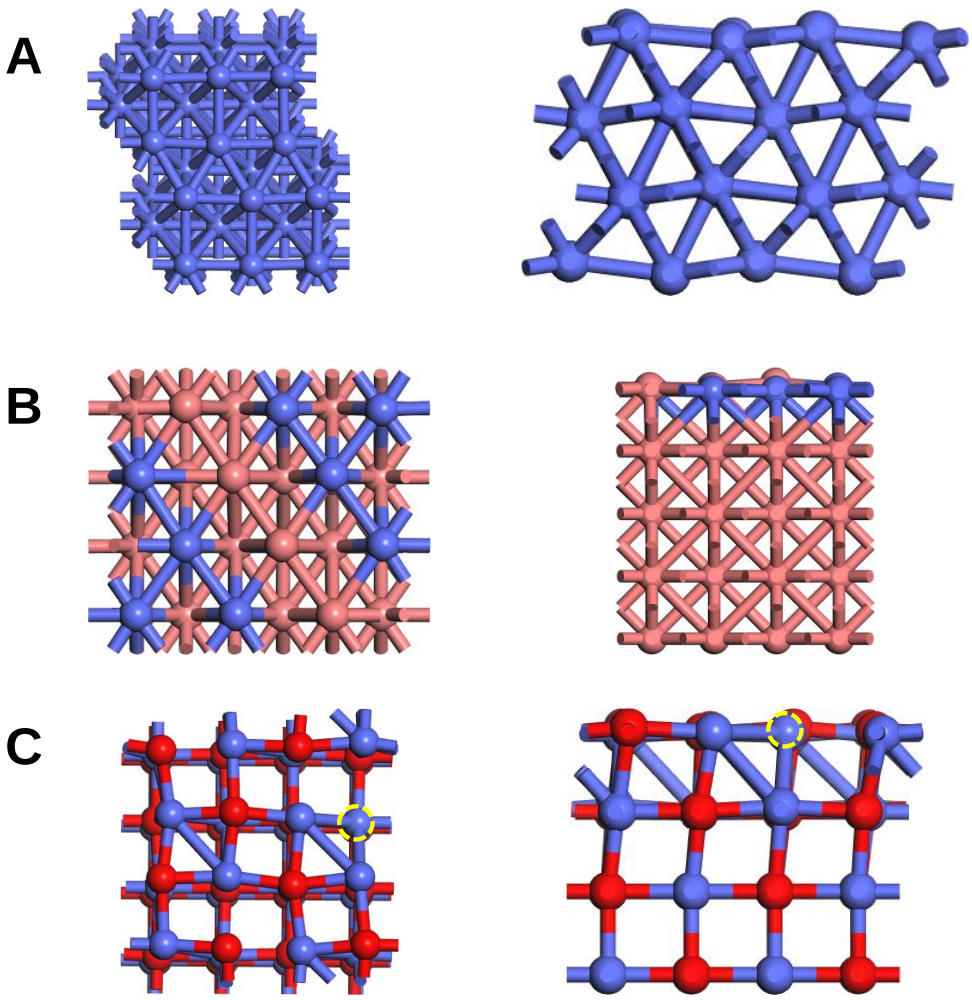

Figure S22. Top (left) and side (right) views of the (A) Co(10-11), (B) Co/Fe(110) and (C) CoO(100) models (additional surface atomic color: O–red). Co is assumed to be in the most stable hcp phase. The CoFe alloy is modeled by partially replacing surface Fe atoms on the most stable Fe(110) slab of the bcc phase. CoO is modeled by its non-polar (100) slab with a surface oxygen vacancy (the yellow circle).

We modeled the Co phase using the Co(10-11) slab surface, as Co exists in the more stable hcp phase. For the CoFe alloy, our experiment suggests it to be in the bcc phase, so we modeled it with the Co/Fe(110) slab surface, as the (110) surface is the most stable one for this phase. For the CoO phase, previous studies suggest that CH_3O dissociation is more favorable at a surface oxygen vacancy site, so we modeled it with the CoO(100) surface with a surface O vacancy. Additionally, CoO was treated as an antiferromagnetic system with a much denser k-point grids for the Brillouin zone.

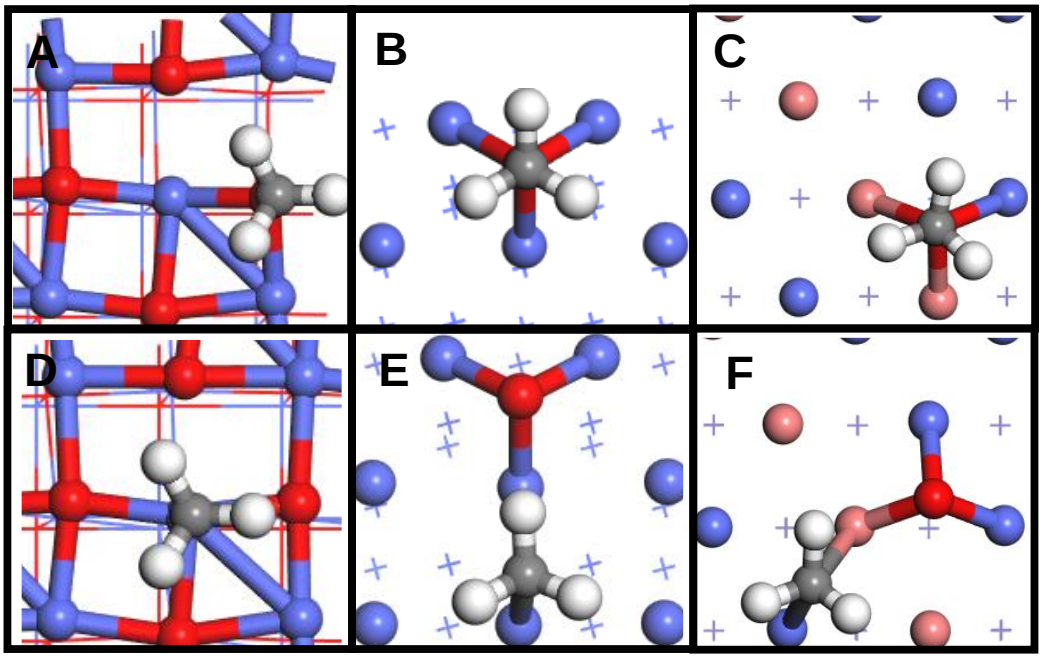

Figure S23. (A–C) Structure of the CH_3O* adsorbate on the (A) CoO(100), (B) Co(10-11) and (C) Co/Fe(110) surface models show in Figure 7. (D–F) The structure after its dissociation into CH_3* and O* on these surfaces.

Supplemental References

1. Nie, X., Meng, L., Wang, H., et al. (2018). DFT insight into the effect of potassium on the adsorption, activation and dissociation of CO_2 over Fe-based catalysts. Phys. Chem. Chem. Phys. ***20***, 14694–14707.
2. Choi, Y.H., Jang, Y.J., Park, H., et al. (2017). Carbon dioxide Fischer-Tropsch synthesis: A new path to carbon-neutral fuels. Appl. Catal., B ***202***, 605-610.
3. Choi, Y.H., Ra, E.C., Kim, E.H., et al. (2017). Sodium-containing spinel zinc ferrite as a catalyst precursor for the selective synthesis of liquid hydrocarbon fuels. ChemSusChem ***10***, 4764-4770.
4. Hwang, S.-M., Han, S.J., Park, H.-G., et al. (2021). Atomically alloyed Fe–Co catalyst derived from a N-coordinated Co single-atom structure for CO_2 hydrogenation. ACS Catal. ***11***, 2267-2278.
5. Yao, B., Xiao, T., Makgae, O.A., et al. (2020). Transforming carbon dioxide into jet fuel using an organic combustion-synthesized Fe-Mn-K catalyst. Nat. Commun. ***11***, 6395.
6. Kwak, J.H., Kovarik, L. and Szanyi, J. (2013). CO_2 reduction on supported Ru/Al_2O_3 catalysts: Cluster size dependence of product selectivity. ACS Catal. ***3***, 2449–2455.
7. Li, S.W., Xu, Y., Chen, Y.F., et al. (2017). Tuning the selectivity of catalytic carbon dioxide hydrogenation over iridium/cerium oxide catalysts with a strong metal-support interaction. Angew. Chem., Int. Ed. ***56***, 10761–10765.
8. Chen, X., Peng, M., Cai, X., et al. (2021). Regulating coordination number in atomically dispersed Pt species on defect-rich graphene for n-butane dehydrogenation reaction. Nat. Commun. ***12***, 2664.
9. Peng, M., Dong, C.Y., Gao, R., et al. (2021). Fully exposed cluster catalyst (FECC): Toward rich surface sites and full atom utilization efficiency. ACS Cent. Sci. *7*, 262–273.
10. Ashworth, D.J., Roseveare, T.M., Schneemann, A., et al. (2019). Increasing alkyl chain length in a series of layered metal-organic frameworks aids ultrasonic exfoliation to form nanosheets. Inorg. Chem. ***58***, 10837–10845.